RESEARCH ARTICLE

CFD Simulation of Gas-Slag-Metal Multiphase Flow in a Side-Blown Vortex Smelting Reduction Reactor

Shuai Zhu[1,2] · Qiuyue Zhao[1,2] · Xiaolong Li[1,2] · Yan Liu[1,2] · Ting'an Zhang[1,2]

Abstract

For the recovery and utilization of valuable metals in metallurgical solid waste, a side-blown vortex smelting reduction reactor is proposed for the recovery of Fe from copper slag. A preliminary numerical simulation of the multiphase flow in the reactor was performed. The effect of nozzle diameter and modified Froude number on the gas-copper slag-iron interaction was investigated. The results show that when the nozzle diameter is identical, with increasing modified Froude number, the motion of the slag surface will be increasingly intense, the slag splashing amount will increase significantly, and the distribution of the gas-slag mixed phase will be increasingly expanded. The generation of vortex flow is related to the gas penetration behavior. When the nozzle diameter is identical, the gas penetration depth increases with increasing the modified Froude number, and the vortex flow gradually generates. When the gas flow rate is identical, the modified Froude number increases with decreasing nozzle diameter, causing the slag splashing amount will slightly increase. When the gas flow rate is identical, the gas penetration depth increases with decreasing nozzle diameter, causing the vortex flow to be more easily generated. When the nozzle diameter and the modified Froude number are constant, the gas–oil–water system forms a vortex flow more easily than the gas-slag-metal system, which is related to the expansion phenomenon of the gas under high-temperature conditions.
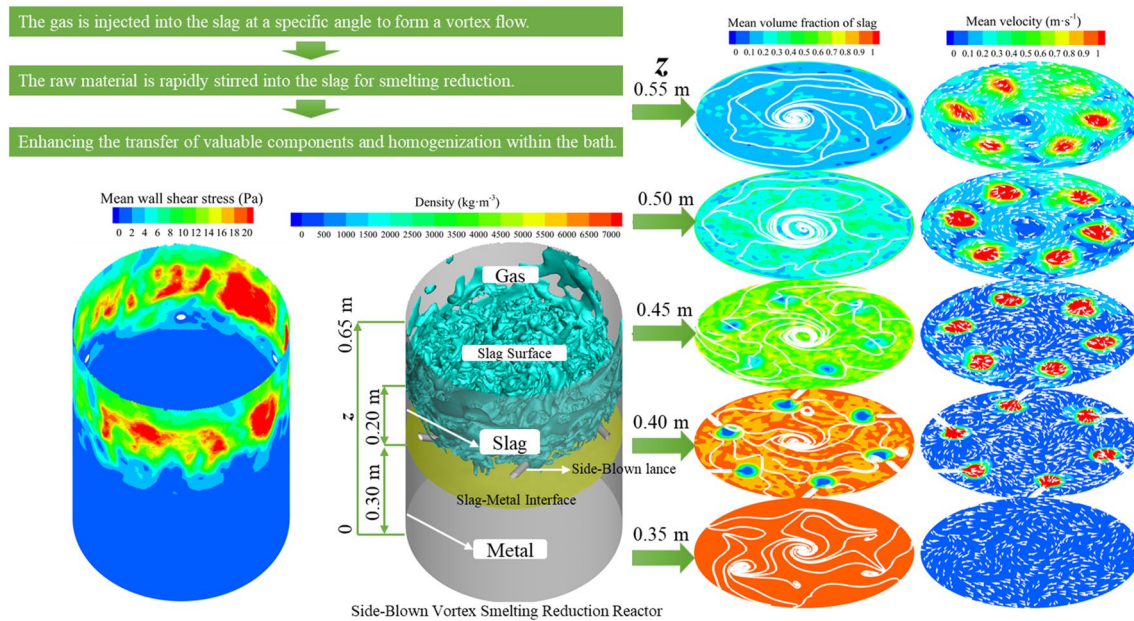
Graphical Abstract

Side-Blown Vortex Smelting Reduction Reactor

Introduction

The metallurgical industry produces a significant amount of solid waste [1], for instance, tens of millions of tons of copper slag and more than 100 million tons of red mud are produced annually [2, 3]. Unfortunately, the current treatment techniques are restrictive, resulting in ineffective recycling and utilization of solid waste. [4]. As a result, the storage of metallurgical solid waste occupies land and causes environmental and safety problems [5, 6]. Exploring resource utilization for metallurgical solid wastes is necessary to address this issue. Copper slag contains several recoverable metals, including Fe, which accounts for about 40 wt.% [7]. Fe in copper slag can be recovered through magnetic separation or high-temperature reduction [8, 9]. Many studies have reported on the recovery of Fe from copper slag using smelting reduction [9–12]. However, the smelting reduction process usually requires specific reactors and involves complex gas-slag-metal interactions [13]. Thus, understanding the flow and interaction of the multiphase system is crucial. Based on the smelting reduction process, a novel side-blown vortex smelting reduction reactor is proposed in this paper to recover Fe from metallurgical waste slags [14, 15].

Multiphase interactions in pyrometallurgical reactors are challenging to observe and measure experimentally. Therefore, numerous numerical studies have been carried out for side-blown reactors. Typically, the VOF multiphase

flow model coupled with the k-ε or k-ω turbulence model is commonly used for this purpose. In the ironmaking field, Stephens et al. [16] simulated the bath dynamics in the HIsmelt process and showed that the numerical model they developed could capture the flow dynamics and clarify the effect of particle number on convergence. Witt et al. [17] simulated the HIsmelt process and showed that including thermal effects in the simulation would increase the computational cost, but that thermal effects were significant for the particle heating rate, gas generation, and dynamics in the bath. Feng et al. [18] simulated a C–H₂ smelting reduction furnace with top-side-bottom combined blowing and showed that the mixing effect, reaction interface, splash, and lining erosion all increased with increasing gas flow rate and immersion depth of the side lance. Bölke et al. [19] and Svantesson et al. [20] simulated the IronArc ironmaking process and showed that in the jet regime, the energy utilization was higher, and the refractory erosion was slower. He et al. [21] simulated an iron bath reactor with side-bottom combined blowing and showed that increasing the inclination angle and immersion depth of the side lance promoted bath mixing. The gas holdup and stirring intensity increased with an increase in the immersion depth of the side lances. Sun et al. [22] simulated the mixing behavior in an iron bath gasifier with top-side-bottom combined blowing and showed that the numerical results were consistent with the experimental

results for the bath's flow pattern and mixing behavior. Bian et al. [23] simulated the ironmaking process with oxygen-rich side-blown for vanadium-titanium magnetite and showed that the gas-slag mixing was uniform, and the fluctuations of the slag-iron interface and the turbulence in the molten iron layer were weak. In the argon oxygen decarburization (AOD) converter field, Odenthal et al. [24] and Wuppermann et al. [25] studied the oscillation problem of the AOD converter. Wei et al. [26, 27] found that the number and angle of tuyeres had less effect on the basic characteristics of gas stirring, liquid flow, and turbulent kinetic energy distribution. Wimmer et al. [28] compared and optimized the various geometries of vessels in detail. Cheng et al. [29] studied the effect of tuyere configuration and gas flow rate on the flow characteristics, and mixing behavior. In the Peirce-Smith converter (PSC) field, Chibwe et al. [30–32] found that top-side combined blowing could improve process efficiency and reduce splashing. Sonic flow conditions could slow down the refractory erosion in the tuyere area. Almaraz et al. [33] found that the bubbling-jetting transition is better represented by the Kutateladze number. Silva et al. [34] evaluated the effect of operating conditions on the service life of refractory materials. Zhao et al. [35] determined the optimal operating parameters by comprehensively considering the circulation flow and wall shear stress. Lu et al. [36] found that periodically changing the nozzle height could evenly scour the furnace lining near the nozzle and prolong the service life. In the oxygen-enriched side-blown reactor field, Zhang et al. [37] simulated the Vanyukov furnace and showed that the slag was more active above the tuyeres. Liu et al. [38] found that a locally compact with globally sparse nozzle layout resulted in better mixing intensity and gas distribution, slowing down the erosion of the furnace lining. Liu et al. [39] found that the gas penetration depth, surface fluctuation height, and bubble scale calculated using the realizable k-ε model agreed with the experimental results. Xiao et al. [40] found that the gas in the copper smelting process was a periodic bubbling pattern.

The proposed novel side-blown vortex smelting reduction reactor can use metallurgical solid wastes, such as copper slag or red mud, for ironmaking. The preheated air is injected into the slag at a specific angle to produce a vortex flow inside the slag which rapidly stirs the raw material (slag with the reducing agent) for smelting and reduction, enhancing the transfer of valuable components and homogenization within the bath. The CO generated by the reduction reaction and the excess C reacted exothermically with the injected air to maintain good slag fluidity. While the mixing behavior and bubble characteristics in the reactor have been studied by physical simulation [14, 15], such experimental studies were limited to the gas–liquid system due to the limitation

of measurement methods, and differ from the actual gas-slag-metal system. Therefore, numerical simulation methods were employed in this study to obtain flow information, explore process conditions, and develop a preliminary model applicable to this reactor. The study investigates gas-slag-metal interaction, and multiphase flow information, and verifies the feasibility of vortex flow generation in the slag driven by gas. This research is of great significance for optimizing the reactor and future industrial practice.

Simulation Methods

Geometry and Mesh Model

It is difficult to obtain valuable information from experiments with a gas-oil–water system. Therefore, both gas-slag-metal and some gas–oil–water systems were simulated. The properties of copper slag vary depending on the smelting process, resulting in a wide range of kinematic viscosity values. The kinematic viscosity of silicone oil (100×10^{-6} $m^2 \cdot s^{-1}$) used to simulate copper slag is relatively close to that of copper slag (62.5×10^{-6} $m^2 \cdot s^{-1}$) in the literature [40]. Because the reactor has not yet been realized for production, the laboratory-scale reactor was simulated. The dimensions of the reactor are detailed in Table 1, while the geometry and mesh model is illustrated in Fig. 1. The simulation focused primarily on the slag layer, where multiphase interactions were most intense. Therefore, local mesh encryption was applied to the nozzle outlet, the middle and upper region of the slag layer, and part of the region above the liquid surface. Figure 2 shows the monitoring planes and monitoring lines. As shown in Fig. 3, the mesh-independent verification of the gas-oil–water system was conducted using mesh numbers 454217, 775813, 962401, and 1098014. The gas expansion could be accurately simulated when the mesh numbers were 962401 and 1098014, which indicated that these two meshes satisfied the requirements for the simulation. Finally, the simulation was carried out with mesh number 962401.

Governing Equations

The fluid flow was simulated with the VOF multiphase flow model coupled with the SST k-ω turbulence model. And the following assumptions were made: (1) gas was regarded as compressible Newtonian fluid and liquids were incompressible; (2) gas viscosity followed Sutherland theory and the physical properties of liquids were constant; (3) fluid flow was a three-dimensional, unsteady, non-isothermal process; (4) chemical reactions were neglected.

In the VOF model, the trace of the interface between the phases is accomplished by solving the continuity equation

Table 1 Dimensions of the reactor and the physical properties of the fluids [40, 41]

Parameters		Values		
Vessel diameter D (m)		0.48		
Vessel height H (m)		0.65		
Lance installation height H_L (m)		0.4045		
Lance submersion depth S_L (m)		0.05		
Tangential angle of the lance α (°)		60		
Vertical angle of the lance β (°)		10		
Height of the metal or water (m)		0.30		
Height of the slag or oil (m)		0.20		
Nozzle diameter d_n (10^{-3} m)		3.00	3.75	4.50
Number of lances n		6		
Temperature T (K)	Gas–oil–water	293		
	Gas-slag-metal	1773		

Physical properties	Gas–oil–water	Values	Gas-slag-metal	Values
Density (kg·m^{-3})	Air	Ideal gas	Air	Ideal gas
	Silicone oil	960	Copper slag	3360
	Water	998	Iron	7036
Viscosity (Pa·s)	Air	1.81×10^{-5}	Air	Sutherland
	Silicone oil	0.096	Copper slag	0.21
	Water	0.001	Iron	0.0075
Surface tension (N·m^{-1})	Silicone oil	0.021	Copper slag	0.32
	Water	0.072	Iron	1.6

Fig. 1 Geometry and mesh model of the reactor
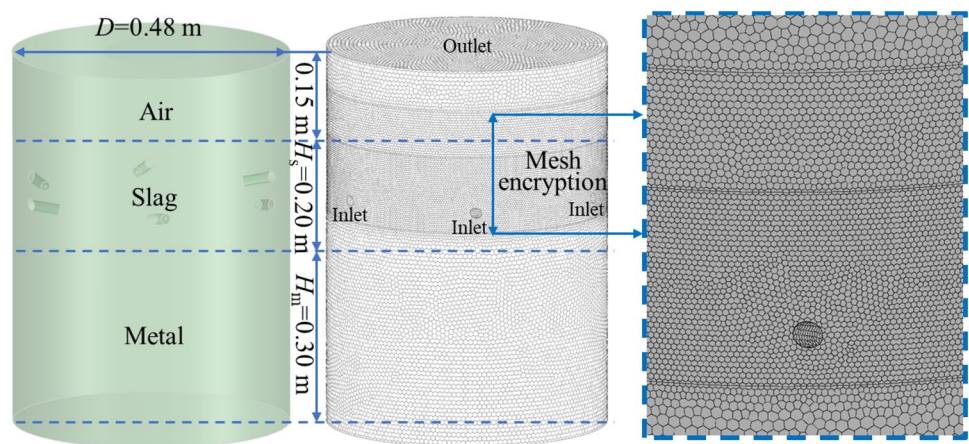
for the volume fraction of the phases. For the qth phase, the equation takes the following form.

$$\frac{1}{\rho_q}\left[\frac{\partial\left(\rho_q\alpha_q\right)}{\partial t} + \nabla\left(\alpha_q\rho_q\overrightarrow{u_q}\right)\right] = 0 \tag{1}$$

where ρ_q, α_q and $\overrightarrow{u_q}$ are the density, volume fraction, and velocity vector of the qth phase, respectively, and

$$\sum_{q=1}^{3}\alpha_q = 1 \tag{2}$$

The momentum equation is shared by each phase and the equation has the following form.

$$\frac{\partial}{\partial t}\left(\rho\vec{u}\right) + \nabla \cdot \left(\rho\vec{u}\vec{u}\right) = -\nabla p + \nabla \cdot \left[\mu\left(\nabla\vec{u} + \nabla\vec{u}^T\right)\right] + \rho\vec{g} + F \tag{3}$$
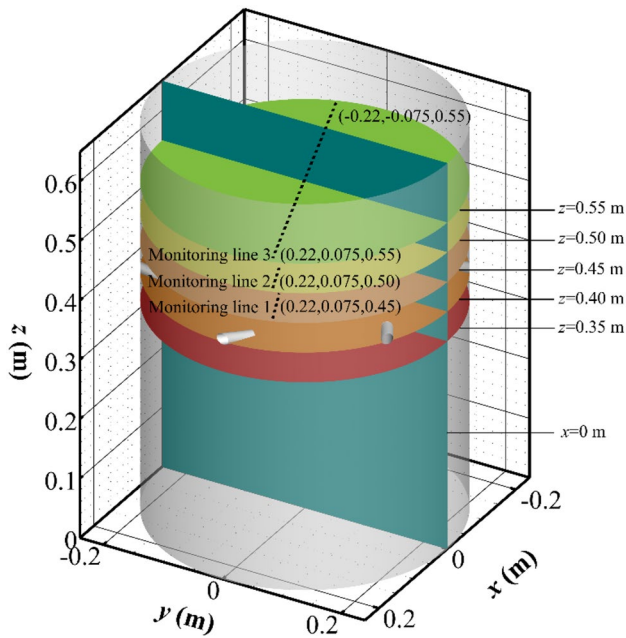
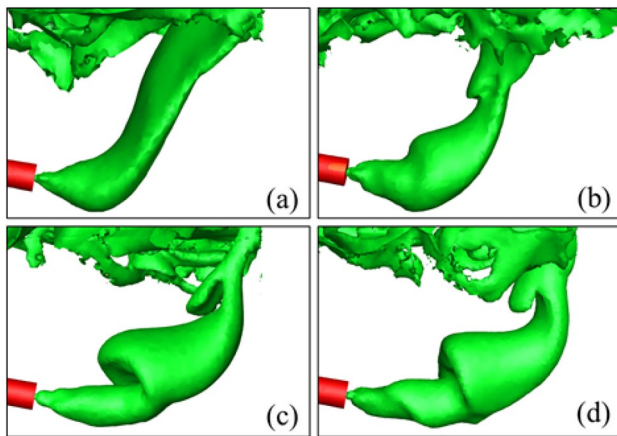**Fig. 2** Monitoring planes and monitoring lines in the reactor

Fig. 3 Simulation results of the gas morphology in oil with the different mesh numbers, $d_n = 3.00$ mm, and $Fr' = 4948$. **a** 454,217; **b** 775,813; **c** 962,401; **d** 1,098,014

where p is the pressure; $\vec{g}$ is the gravity vector; ρ and μ are the density and viscosity of the mixture; F is the interfacial tension, and

$$\rho = \sum_{q=1}^{3} \alpha_q \rho_q \tag{4}$$

$$\mu = \sum_{q=1}^{3} \alpha_q \mu_q \tag{5}$$

$$F = \sum_{pairs\, qr,\, q<r\leq 3} \sigma_{qr} \frac{\alpha_q \rho_q c_r \nabla \alpha_r + \alpha_r \rho_r c_q \nabla \alpha_q}{0.5(\rho_q + \rho_r)} \tag{6}$$

where σ_{qr} is the interfacial tension between the qth and rth phases; c is the curvature of the phase interface.

The energy equation is shared by each phase and the equation has the following form.

$$\frac{\partial}{\partial t}(\rho E) + \nabla \cdot [\vec{u}(\rho E + p)] = \nabla \cdot (\lambda_{\text{eff}} \nabla T) \tag{7}$$

where T is the temperature; E is the energy, treated as a mass-averaged variable; λ_{eff} is the effective thermal conductivity, and

$$\lambda = \sum_{q=1}^{3} \alpha_q \lambda_q \tag{8}$$

$$E = \sum_{q=1}^{3} \alpha_q \rho_q E_q \Big/ \sum_{q=1}^{3} \alpha_q \rho_q \tag{9}$$

The SST k-ω turbulence model is a hybrid model that has been widely used in engineering, retaining the original k-ω model in the region near the wall and applying the k-ε model in the region away from the wall. svantesson et al. [22] applied the SST k-ω model in a study of submerged side-blown gas and obtained relatively accurate results. The turbulent kinetic energy k and the specific dissipation rate ω are obtained from the following transport equations.

$$\frac{\partial(\rho k)}{\partial t} + \frac{\partial(\rho k u_i)}{\partial x_i} = \frac{\partial}{\partial x_j}\left[\left(\mu + \frac{\mu_t}{\sigma_k}\right)\frac{\partial k}{\partial x_j}\right] + G_k - Y_k + G_b \tag{10}$$

$$\frac{\partial(\rho \omega)}{\partial t} + \frac{\partial(\rho \omega u_i)}{\partial x_i} = \frac{\partial}{\partial x_j}\left[\left(\mu + \frac{\mu_t}{\sigma_\omega}\right)\frac{\partial \omega}{\partial x_j}\right] + G_\omega - Y_\omega + D_\omega + G_{\omega b} \tag{11}$$

where μ_t is the turbulent viscosity; G_k is the generation of turbulence kinetic energy due to mean velocity gradients; G_ω is the generation of ω; Y_k and Y_ω are the dissipation of k and ω due to turbulence, respectively; D_ω is the cross-diffusion term; G_b and $G_{\omega b}$ are the turbulent kinetic energy generated by buoyancy.

$$\mu_t = \frac{\rho k}{\omega} \frac{1}{\max\left[\frac{1}{\alpha^*}, \frac{S \tanh(\phi_2^2)}{a_1 \omega}\right]} \tag{12}$$

where S is the strain rate magnitude, and

$$\alpha^* = \alpha_\infty^* \left(\frac{\alpha_0^* + \rho k / \mu \omega R_k}{1 + \rho k / \mu \omega R_k}\right) \tag{13}$$

$$\phi_2 = \max \left[2\frac{\sqrt{k}}{0.09\omega y}, \frac{500\mu}{\rho y^2 \omega} \right] \tag{14}$$

where y is the distance to the next surface. The model parameters are: $\alpha_0^* = \beta_i/3$, $\alpha_\infty^* = 1$, $\beta_{i.1} = 0.075$, $\beta_{i.2} = 0.0828$, $\sigma_{k.1} = 1.176$, $\sigma_{\omega.1} = 2.0$, $\sigma_{k.2} = 1.0$, $\sigma_{\omega.2} = 1.168$, $a_1 = 0.31$, $R_k = 6$, respectively.

Boundary Conditions and Numerical Methods

The physical properties of the fluids are detailed in Table 1. The simulation was based on ANSYS Fluent. The inlet and outlet were mass flow rate inlet and pressure outlet, respectively. The criterion of modified Froude number Fr' equality determined the gas flow rates for the gas-slag-metal system. No-slip wall conditions were used, and standard wall functions were used to treat the flow in the region near the wall. The pressure−velocity decoupling was achieved using the PISO algorithms. The PRESTO! scheme was used to interpolate the pressure values. The Compressive scheme was used to track the free surface deformation. The transport equations were discretized using the second-order upwind scheme for the convective terms. The time step was set to 5×10^{-5} s. The Patch command was used to define the initial three-phase region. The convergence criterion was that the residual of energy was less than 1×10^{-6} and the residual of other variables was less than 1×10^{-3}. Given the higher computational cost, 10 s were simulated for each case. It should be noted that the fluid flow in the reactor was approximately

periodic and varied drastically within one period. Comparing flow information based on time averaging is more significant than that based on transients [13]. Therefore, time-averaged statistics for important parameters were performed at a later stage of the simulation.

$$Fr' = \frac{\rho_g u_g^2}{(\rho_l - \rho_g)gd_n} \tag{15}$$

$$u_g = \frac{Q_s}{\frac{\pi}{4}d_n^2} \tag{16}$$

$$Fr_a' = Fr_m' \tag{17}$$

where ρ_g and ρ_l are the density of the gas and the density of the liquid, $kg \cdot m^{-3}$, respectively; u_g is the gas apparent velocity at the nozzle outlet, $m \cdot s^{-1}$; Q_s is the gas flow rate of a single lance, $m^3 \cdot h^{-1}$; Fr_a' is modified Froude number of the gas-slag-metal system; Fr_m' is modified Froude number of the gas-oil–water system.

Results and Discussion

Verification of Experimental and Simulation Results

The key factor in the fluid flow in the reactor is the motion state of the side-blown gas. Since the gas mainly affects the slag region, the morphology of side-blown gas in oil was

Fig. 4 Experimental and simulated results of the morphology of side-blown gas in silicone oil, $d_n = 3.00$ mm, $t = 1$ s. **a** $Fr' = 696$; **b** $Fr' = 1336$; **c** $Fr' = 2347$; **d** $Fr' = 3635$; **e** $Fr' = 4948$
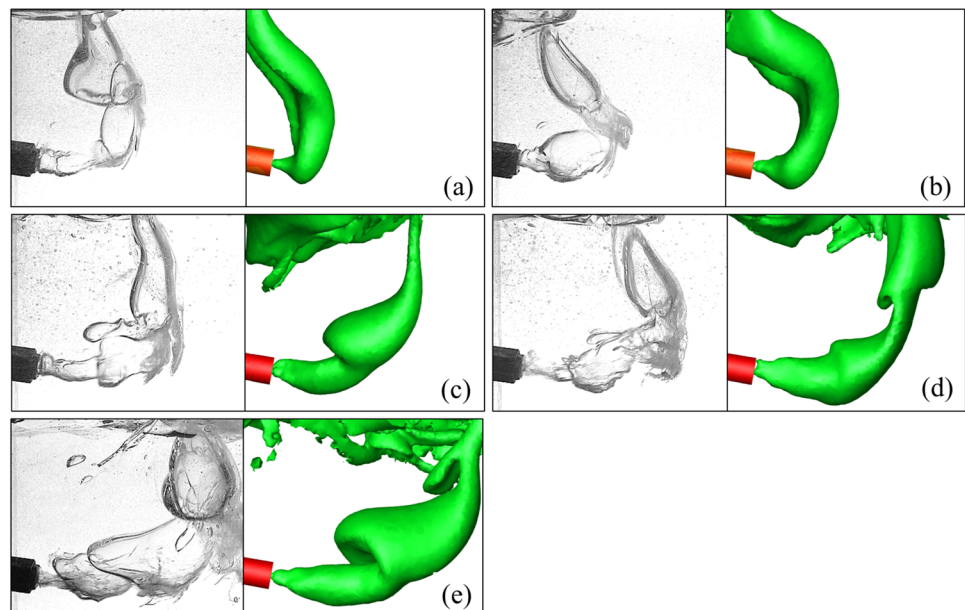
studied experimentally and simulated using the air-silicone oil system, and experimental and simulated results were compared. Figure 4 shows the experimental and simulation results with different Fr' for simulation time $t = 1$ s and $d_n = 3.00$ mm. The materials used in the experiments and simulations in Fig. 4 are identical, both air and silicone oil, and the operating conditions are also completely identical. The simulated results are very close to the experimental results for various Fr'. The numerical models also successfully simulated the gas expansion phenomenon that occurs at higher Fr'. According to the experimental and simulated results, the gas penetration depth will become larger with increasing Fr'. The gas will gradually appear to expand after leaving the nozzle outlet with increasing Fr'. Therefore, the comparison results in Fig. 4 show that the numerical model used in the current study is reliable.

Surface Morphology of the Slag Phase

Figure 5 shows the variation of the surface morphology of the slag with time. It can be seen that the interaction between the gas and the slag will become more and more intense with time, and the action range of the gas gradually extends to the whole surface. Figure 6 shows the surface morphology of the slag with various operating conditions. First, it can be seen from Fig. 6a–d that the motion state of the slag surface will change from a relatively stable state to a highly violent state with increasing Fr' as $d_n = 3.00$ mm. The gas action region gradually expands from the slag surface above the nozzle to the whole surface with increasing Fr'. The violent gas-slag interaction causes the liquid surface to gradually splash with increasing Fr'. It indicates that the effect of total gas flow

rate Q on the gas-slag interaction is very significant. Second, although Fr' decreases with increasing nozzle diameter when the gas flow rate is identical ($Q = 97.20$ m$^3 \cdot$h^{-1}), the slag surface motion in all three cases in Fig. 6c, e and f is very violent and the difference is not significant. It may be that in the high-temperature system, the expansion of the gas is very significant, resulting in a more significant splashing when it escapes from the surface. Therefore, it caused the surface motion to be very violent under all three nozzle diameters.

Figure 7 shows the slag splashing amount with various operating conditions. By compiling the User Defined Function, the slag amount above the slag surface and the total slag amount in the reactor are obtained, and the ratio is the slag splashing amount. When $d_n = 3.00$ mm, the slag splashing amount increases significantly with increasing Fr', indicating that the gas flow rate is an essential factor affecting the splashing. When Q is identical, the slag splashing amount will slightly decrease because increasing nozzle diameter will lead to decreasing Fr'.

Volume Distribution of the Slag Phase

Figure 8 shows the mean volume fraction of the slag phase at the monitoring plane $x = 0$ with various operating conditions. First, the motion of the gas and slag has a relatively weak effect on the metal phase under the current operating conditions. The slag-metal interface is very stable. The motion of the gas affects mainly the middle and upper regions of the slag layer. Second, Fig. 8a–d shows that the distribution range of the mixed phase of gas and slag (the green area in Fig. 8) gradually increases with increasing Fr' as $d_n = 3.00$ mm. The mixed phase distribution region
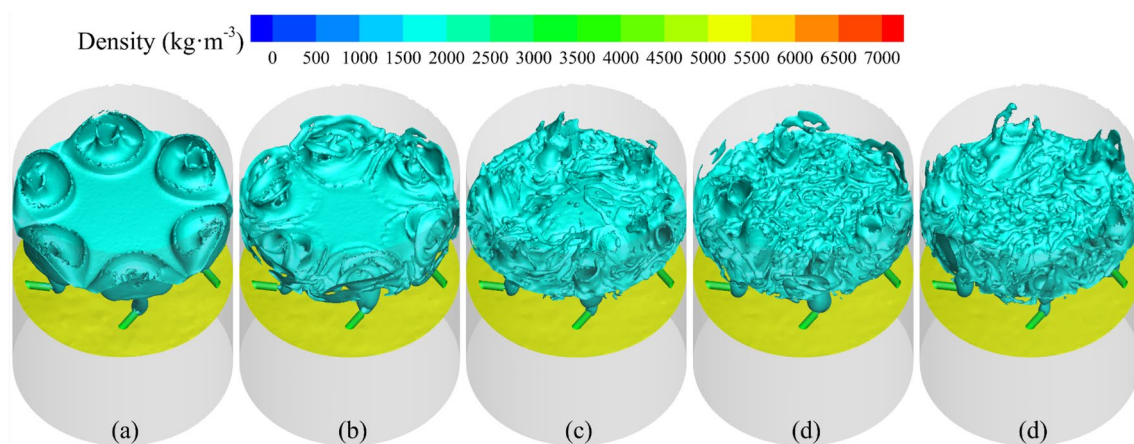

Fig. 5 Variation of the surface morphology of the slag with time, $d_n = 3.00$ mm and $Fr' = 2347$. **a** $t = 0.5$ s; **b** $t = 1.0$ s; **c** $t = 1.5$ s; **d** $t = 2.0$ s; **e** $t = 2.5$ s
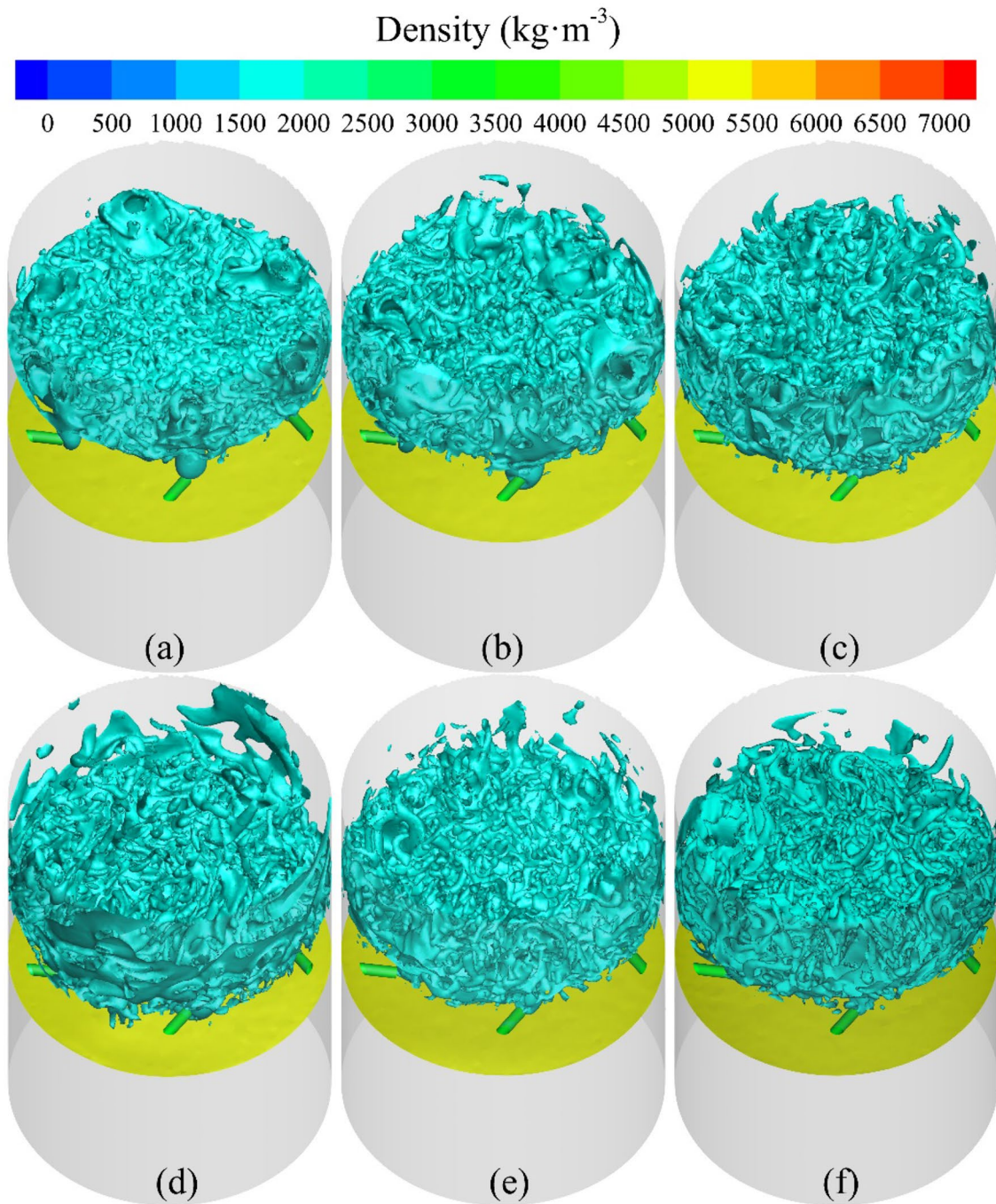
Fig. 6 Surface morphology of the slag. **a** $d_n = 3.00$ mm, $Fr' = 696$; **b** $d_n = 3.00$ mm, $Fr' = 2347$; **c** $d_n = 3.00$ mm, $Fr' = 4948$; **d** $d_n = 3.00$ mm, $Fr' = 7228$; **e** $d_n = 3.75$ mm, $Fr' = 1621$; **f** $d_n = 4.50$ mm, $Fr' = 652$

gradually expands downward to the middle of the slag layer and upward above the initial liquid surface ($z = 0.50$ m) of the slag layer with increasing Fr', respectively. Third, Fig. 8c, e and f show that although Q is identical, decreasing d_n leads to an increase in Fr', which causes the mixed phase distribution region to gradually expand. Fourth, Fig. 8 also shows that increasing Fr' or decreasing d_n also causes increasingly intense splashing on the slag surface.

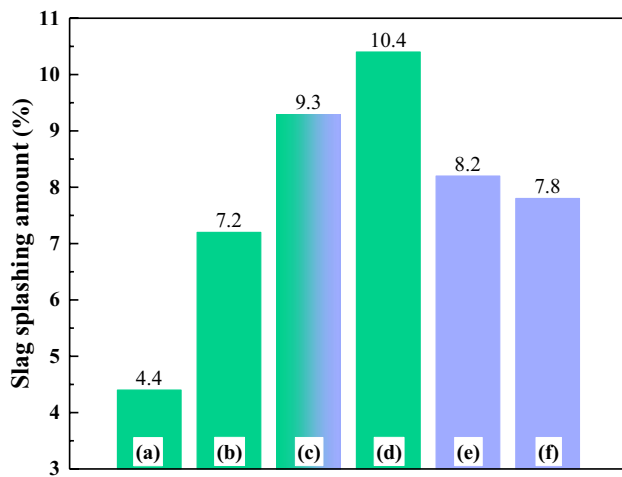Figure 9 shows the mean volume fraction of the slag phase at the monitoring planes in the z-direction with

Fig. 7 Slag splashing amount. **a** $d_n = 3.00$ mm, $Fr' = 696$; **b** $d_n = 3.00$ mm, $Fr' = 2347$; **c** $d_n = 3.00$ mm, $Fr' = 4948$; **d** $d_n = 3.00$ mm, $Fr' = 7228$; **e** $d_n = 3.75$ mm, $Fr' = 1621$; **f** $d_n = 4.50$ mm, $Fr' = 652$

various operating conditions. First, since the main region of gas action is the middle and upper regions of the slag layer, the mean volume fraction of the slag phase at the monitoring plane $z = 0.45$ m and $z = 0.50$ m will decrease. Second, Fig. 9a–d show that when d_n is identical, the gas distribution in the slag will gradually expand to the monitoring plane $z = 0.40$ m as Fr' increases from 696 to 7228. It indicates that when d_n is identical, increasing Fr' is essential to improve the action range of gas and the interface area, as well as accelerate the reaction between gas and slag. Third, the distribution of the streamlines in Fig. 9a–d shows that the vortex motion driven by the submerged side-blown gas can be generated in the slag as Fr' increases, and the vortex motion will become more and more significant with increasing Fr'. Figure 10a shows the streamlines and the mean volume fraction of oil at the monitoring plane in the z-direction as $Fr' = 4948$ for the gas-oil–water system. Figure 9c and Fig. 10a show that when Fr' is identical, the vortex motion generated in the gas-oil–water system will be more significant compared to the gas-slag-metal system. The generation of vortex motion mainly depends on the gas penetration behavior in the horizontal direction, while the gas jet penetration behavior in the gas-oil–water and gas-slag-metal systems is significantly different. Figure 9c and Fig. 10a show that the gas penetration depth in oil is significantly greater than that in slag when Fr' is identical at the monitoring plane $z = 0.40$ m. The reason for this phenomenon is certainly related to the difference in physical properties between slag and oil, but the main reason

seems to be related to the expansion of the gas at high-temperature conditions. In the gas-slag-metal system, the gas is injected into the melt and will expand due to the increase in temperature. Compared with the gas-oil–water system, the initial kinetic energy will be converted into buoyancy energy more quickly in the gas-slag-metal system, resulting in a smaller gas penetration depth. Therefore, although Fr' is identical, the gas-oil–water system more easily forms a vortex flow compared to the gas-slag-metal system. Fourth, Fig. 9c, e and f show that decreasing d_n will increase Fr' for the identical Q, causing vortex flow in the slag to be more easily generated.

Figure 11 shows the horizontal penetration depth of gas with various operating conditions. The gas penetration depth is determined by the state of the phase distribution of the gas jet in the vertical plane where the lance is located and is bounded by a contour with a gas volume fraction of 0.5. First, the penetration depth of the side-blown gas gradually increases with increasing Fr'. Second, although Q is identical, the penetration depth of the side-blown gas is gradually decreasing because the increasing d_n leads to the decreasing Fr'. In summary, the generation of vortex flow in the reactor is mainly dependent on the penetration behavior of the side-blown gas. Therefore, appropriately increasing Fr' can increase the gas penetration depth, which in turn can better promote the generation of vortex flow.

Velocity Fields

Figure 12 shows the mean velocity distribution at the monitoring planes in the z-direction with various operating conditions. First, the mean velocity distribution at the monitoring plane $z = 0.35$ m (slag below the lance) is small when Fr' is identical, indicating that the effect of the gas on the slag below the lance is relatively weak. The mean velocity distribution becomes increasingly larger and more uniform with increasing z. The region with the largest mean velocity (the red region with mean velocity ≥ 1.0 m·s^{-1}) is in the motion region of the main body of the gas. The mean velocity gradually decreases from the red region to the outside, and the closer to the reactor center the mean velocity decreases. Second, Fig. 12a–d shows that the mean velocity distribution in the upper and middle regions of the slag layer ($z > 0.35$ m) becomes more and more uniform with increasing Fr' when $d_n = 3.00$ mm, indicating that increasing Fr' is very significant for strengthening the gas-slag interaction in the upper and middle regions of the slag layer. From the perspective of the distribution of the velocity vector, the vortex flow is gradually formed in the slag layer with increasing

Fig. 8 Mean volume fraction of the slag at the monitoring plane $x=0$. **a** $d_n=3.00$ mm, $Fr'=696$; **b** $d_n=3.00$ mm, $Fr'=2347$; **c** $d_n=3.00$ mm, $Fr'=4948$; **d** $d_n=3.00$ mm, $Fr'=7228$; **e** $d_n=3.75$ mm, $Fr'=1621$; **f** $d_n=4.50$ mm, $Fr'=652$
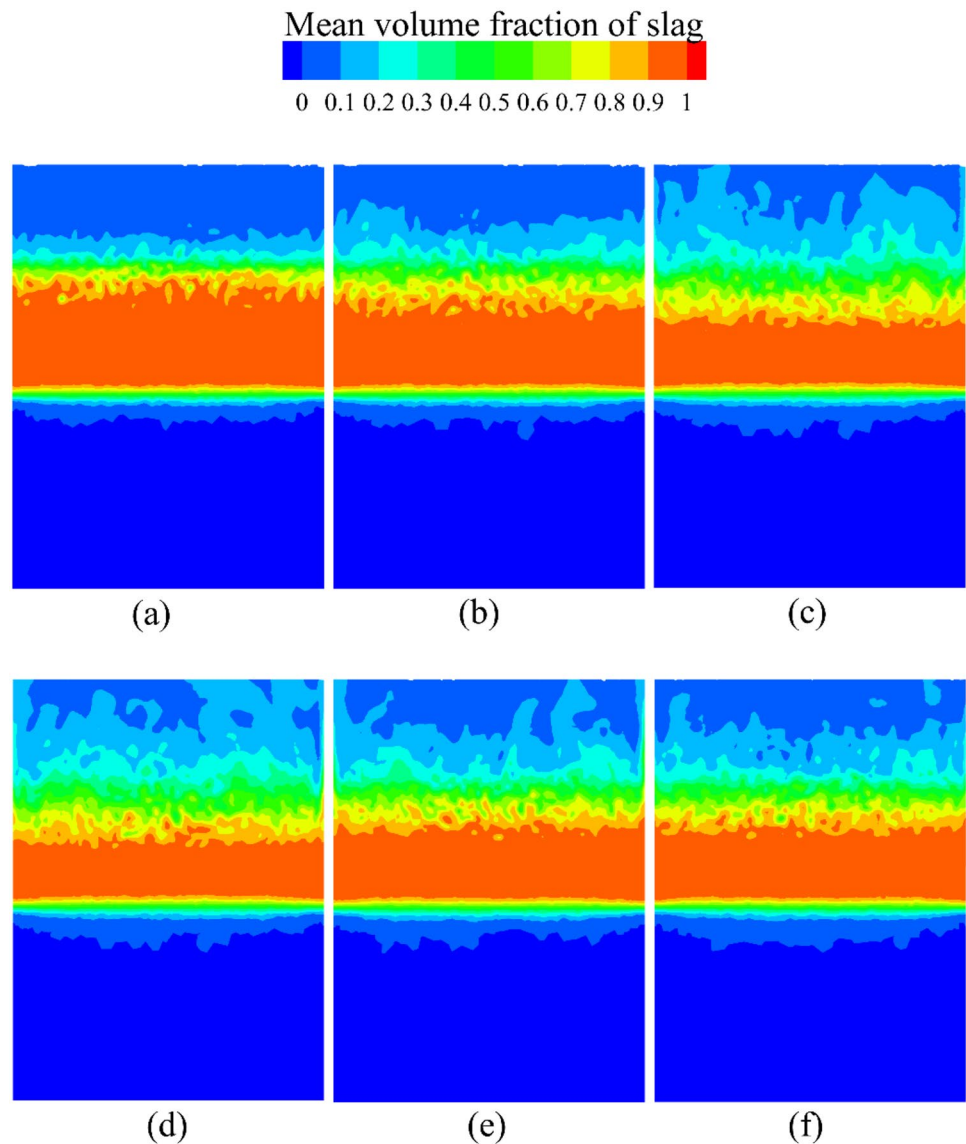

Fr'. It is fully indicated that a larger Fr' is significant for the generation of vortex flow. Figure 10b shows the mean velocity distribution at the monitoring plane in the z-direction as $Fr'=4948$ for the gas-oil–water system. A comparison of Fig. 10b and Fig. 12c shows that although Fr' is identical, the expansion of the gas under high-temperature conditions leads to a significant difference between the vortex flow generated in the gas-slag-metal system and that generated in the gas–oil–water system. The main difference is that the velocity distribution of the vortex flow generated in the gas–oil–water system is more uniform and the vortex flow is more significant. It is a significant difference between the simulation results for the gas-oil–water and gas-slag-metal

systems. Third, Fig. 12c, e and f show that decreasing d_n leads to an increase in Fr' for the identical Q, allowing a more significant vortex flow to be generated in the slag.

The relative standard deviation of the velocity indicates the mixing uniformity in the middle and upper regions of the slag layer [40]. Figure 13 shows the relative standard deviation of the velocity of the region between the monitoring plane $z=0.40$ m and $z=0.50$ m with various operating conditions. By compiling the User Defined Function, the relative standard deviation of velocity is obtained. When $d_n=3.00$ mm, the relative standard deviation of velocity gradually decreases with the increasing Fr', and the mixing uniformity increases. When Q is identical, the relative

Fig. 9 Mean volume fraction of the slag at the monitoring plane in the z-direction. **a** $d_n = 3.00$ mm, $Fr' = 696$; **b** $d_n = 3.00$ mm, $Fr' = 2347$; **c** $d_n = 3.00$ mm, $Fr' = 4948$; **d** $d_n = 3.00$ mm, $Fr' = 7228$; **e** $d_n = 3.75$ mm, $Fr' = 1621$; **f** $d_n = 4.50$ mm, $Fr' = 652$
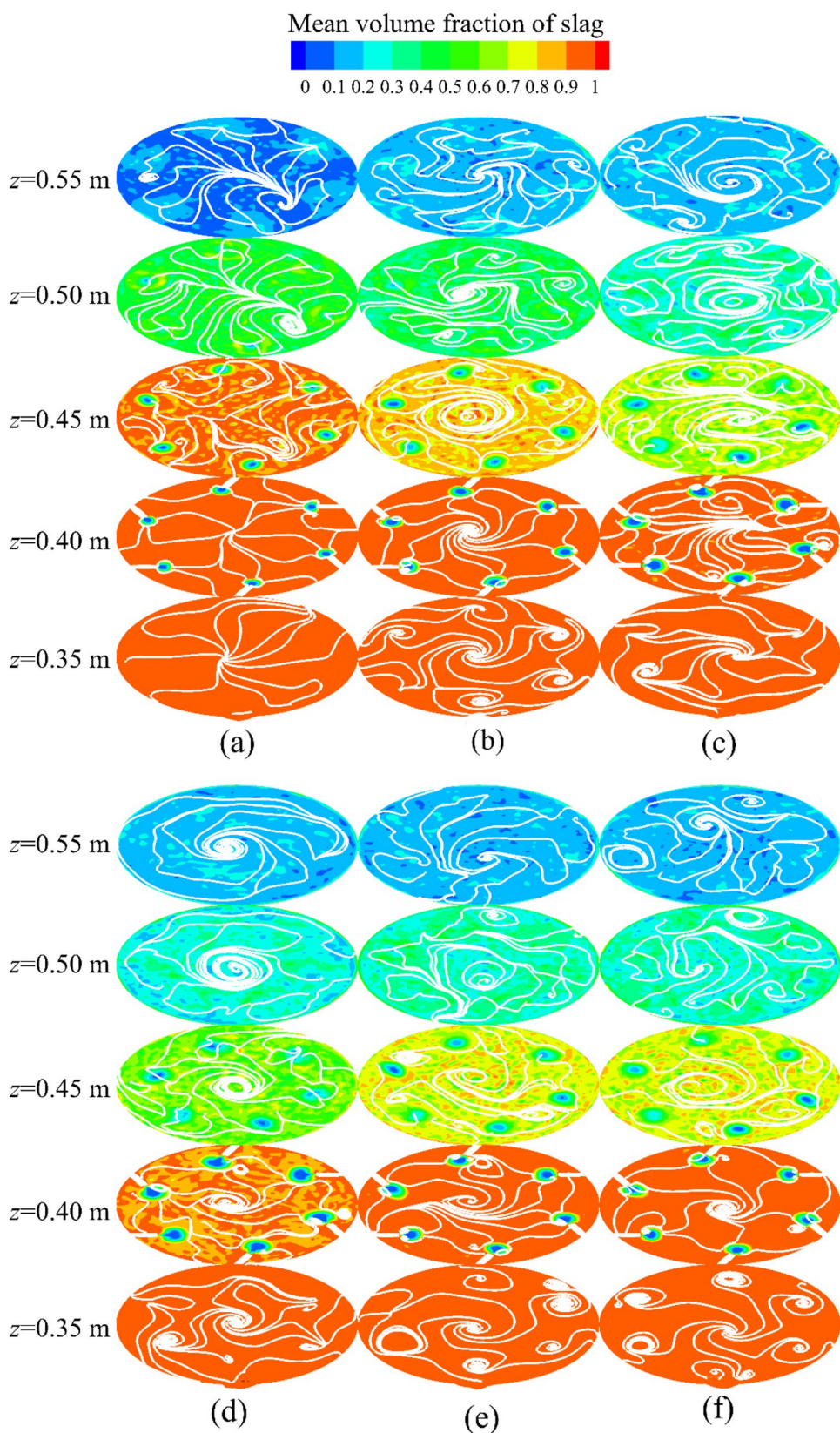
Fig. 10 **a** Mean volume fraction of the oil at the monitoring plane in the z-direction, $d_n = 3.00$ mm, $Fr' = 4948$; **b** Mean velocity distribution at the monitoring plane in the z-direction, $d_n = 3.00$ mm, $Fr' = 4948$
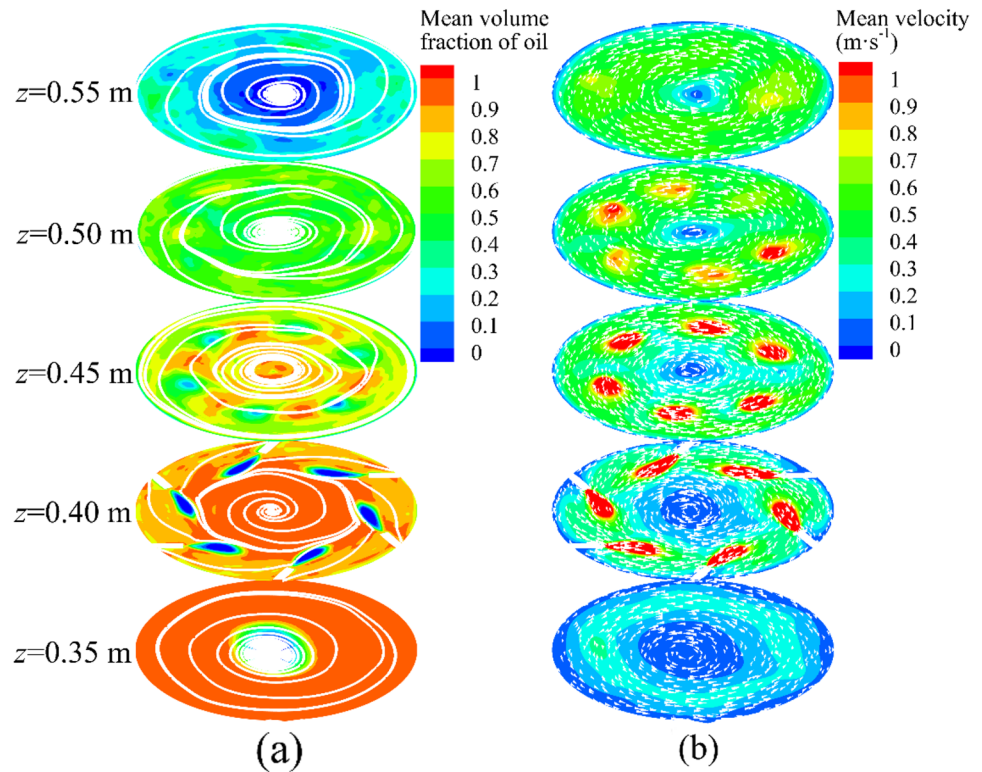
standard deviation of velocity will gradually increase and the mixing uniformity will decrease because increasing nozzle diameter will lead to decreasing Fr'.
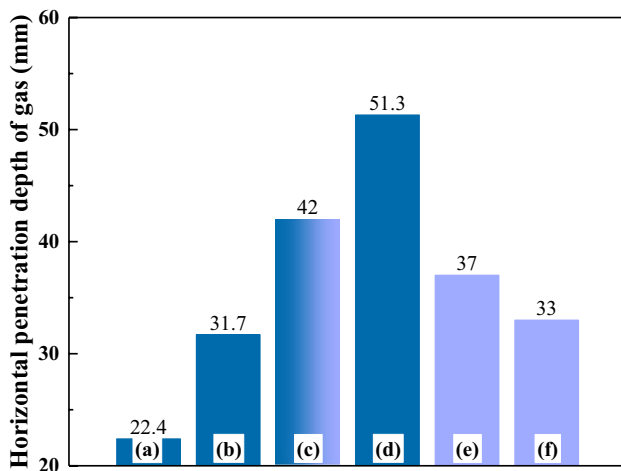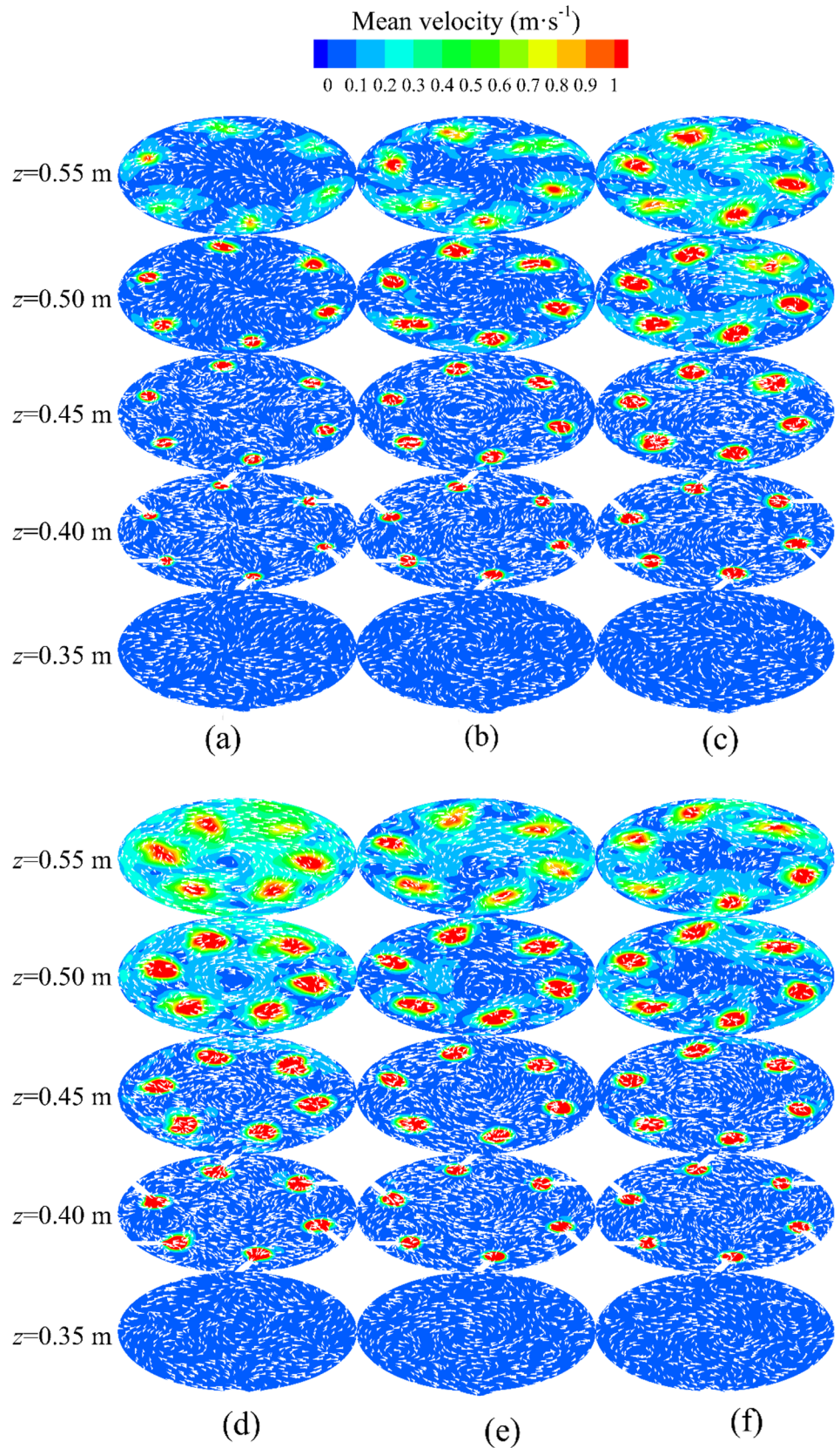

Fig. 11 Horizontal penetration depth of gas. **a** $d_n = 3.00$ mm, $Fr' = 696$; **b** $d_n = 3.00$ mm, $Fr' = 2347$; **c** $d_n = 3.00$ mm, $Fr' = 4948$; **d** $d_n = 3.00$ mm, $Fr' = 7228$; **e** $d_n = 3.75$ mm, $Fr' = 1621$; **f** $d_n = 4.50$ mm, $Fr' = 652$

Figure 14 shows the mean velocity distribution at the monitoring lines. First, the mean velocity shows a double-peaked state with increasing x. The peaks of velocity appear at the position where the main body of the gas passes, and the closer to the reactor center ($x = 0$ m), the smaller the mean velocity of the fluid. Second, the peak of the mean velocity becomes lower with increasing z, but the mean velocity at the position close to the reactor center will increase. It means that the motion of the upper region of the slag phase is greatly affected by the gas. Third, the mean velocity on the monitoring lines is increasing with the increasing Fr' when $d_n = 3.00$ mm. Fourth, Increasing d_n leads to a decrease in Fr' for the identical Q, so the mean velocity (particularly at $z = 0.45$ m) decreases gradually with increasing d_n.

Distribution of Shear Stress on the Side Wall

Figure 15 shows the mean shear stress on the side wall with various operating conditions. First, the shear stress is mainly present on the lining of the slag layer, since the gas mainly affects the upper and middle regions of the slag layer. Therefore, the lining in the region above the lance is more easily eroded. Second, Fig. 15a–d shows that the

Fig. 12 Mean velocity distribution at the monitoring plane in the *z*-direction. **a** $d_n = 3.00$ mm, $Fr' = 696$; **b** $d_n = 3.00$ mm, $Fr' = 2347$; **c** $d_n = 3.00$ mm, $Fr' = 4948$; **d** $d_n = 3.00$ mm, $Fr' = 7228$; **e** $d_n = 3.75$ mm, $Fr' = 1621$; **f** $d_n = 4.50$ mm, $Fr' = 652$
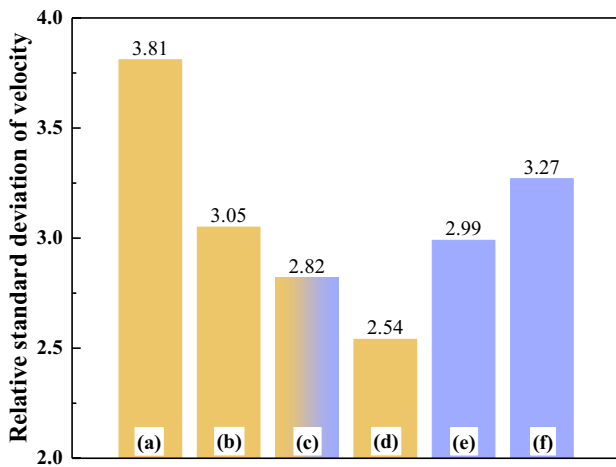
Fig. 13 Relative standard deviation of the velocity. **a** $d_n = 3.00$ mm, $Fr' = 696$; **b** $d_n = 3.00$ mm, $Fr' = 2347$; **c** $d_n = 3.00$ mm, $Fr' = 4948$; **d** $d_n = 3.00$ mm, $Fr' = 7228$; **e** $d_n = 3.75$ mm, $Fr' = 1621$; **f** $d_n = 4.50$ mm, $Fr' = 652$
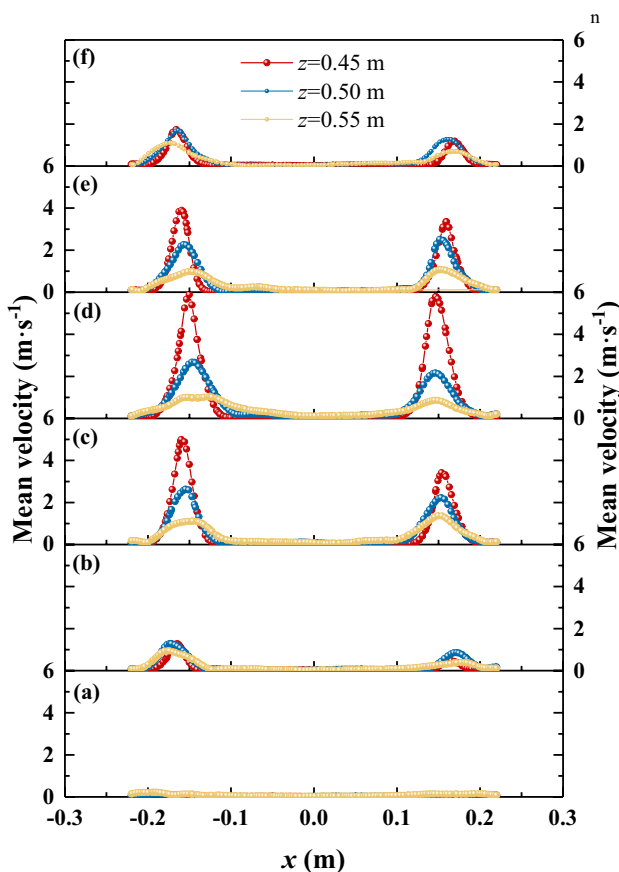

Fig. 14 Mean velocity distribution at the monitoring lines. **a** $d_n = 3.00$ mm, $Fr' = 696$; **b** $d_n = 3.00$ mm, $Fr' = 2347$; **c** $d_n = 3.00$ mm, $Fr' = 4948$; **d** $d_n = 3.00$ mm, $Fr' = 7228$; **e** $d_n = 3.75$ mm, $Fr' = 1621$; **f** $d_n = 4.50$ mm, $Fr' = 652$

erosion of the furnace lining becomes more and more serious with increasing Fr' when $d_n = 3.00$ mm. It indicates that with increasing Fr', the liquid surface and splashing amount will continuously rise, while the motion of the slag layer becomes increasingly violent, resulting in increasingly serious erosion of the furnace lining. Third, Fig. 15c, e and f show that although Q is identical, increasing d_n leads to a decrease in gas penetration depth, which causes the gas-slag interaction near the lining to be more violent and increases the shear stress.

Conclusions

In this paper, a preliminary numerical simulation was performed for the multiphase flow in a side-blown vortex smelting reduction reactor. The effects of nozzle diameter d_n and modified Froude number Fr' on the multiphase interactions were investigated. Information on the multiphase flow was obtained and the feasibility of the gas-driven slag to generate vortex flow was verified. The main conclusions are as follows.

(1) When d_n is identical, the motion of the slag surface will become increasingly intense and the slag splashing amount will increase significantly with increasing Fr'. When d_n is identical, the distribution range of the mixed phase of gas and slag will be extended downward to the middle of the slag layer and upward to above the initial slag surface with increasing Fr', respectively. The generation of vortex flow is related to the gas penetration behavior. When d_n is identical, with increasing Fr', the gas penetration depth increases and the slag gradually forms a vortex flow driven by the side-blown gas. When d_n is identical, with increasing Fr', the erosion of the furnace lining will become more and more serious.

(2) When Q is identical, Fr' increases as d_n decreases, causing the slag splashing amount will slightly increase, and the distribution range of the mixed phase of gas and slag will gradually expand. When Q is identical, the gas penetration depth increases with decreasing d_n, causing the slag to form a vortex flow more easily. When Q is identical, increasing d_n will lead to a decrease in gas penetration depth, which causes the gas-slag interaction near the furnace lining to be more intense and increases the erosion of the furnace lining.

(3) For constant d_n and Fr', the gas-oil–water system forms a vortex flow more easily than the gas-slag-metal system. It is related to the difference in physical properties between slag and oil as well as the expansion phenomenon of gas at high-temperature conditions.

Fig. 15 Mean shear stress on the side wall of the reactor. **a** $d_n = 3.00$ mm, $Fr' = 696$; **b** $d_n = 3.00$ mm, $Fr' = 2347$; **c** $d_n = 3.00$ mm, $Fr' = 4948$; **d** $d_n = 3.00$ mm, $Fr' = 7228$; **e** $d_n = 3.75$ mm, $Fr' = 1621$; **f** $d_n = 4.50$ mm, $Fr' = 652$
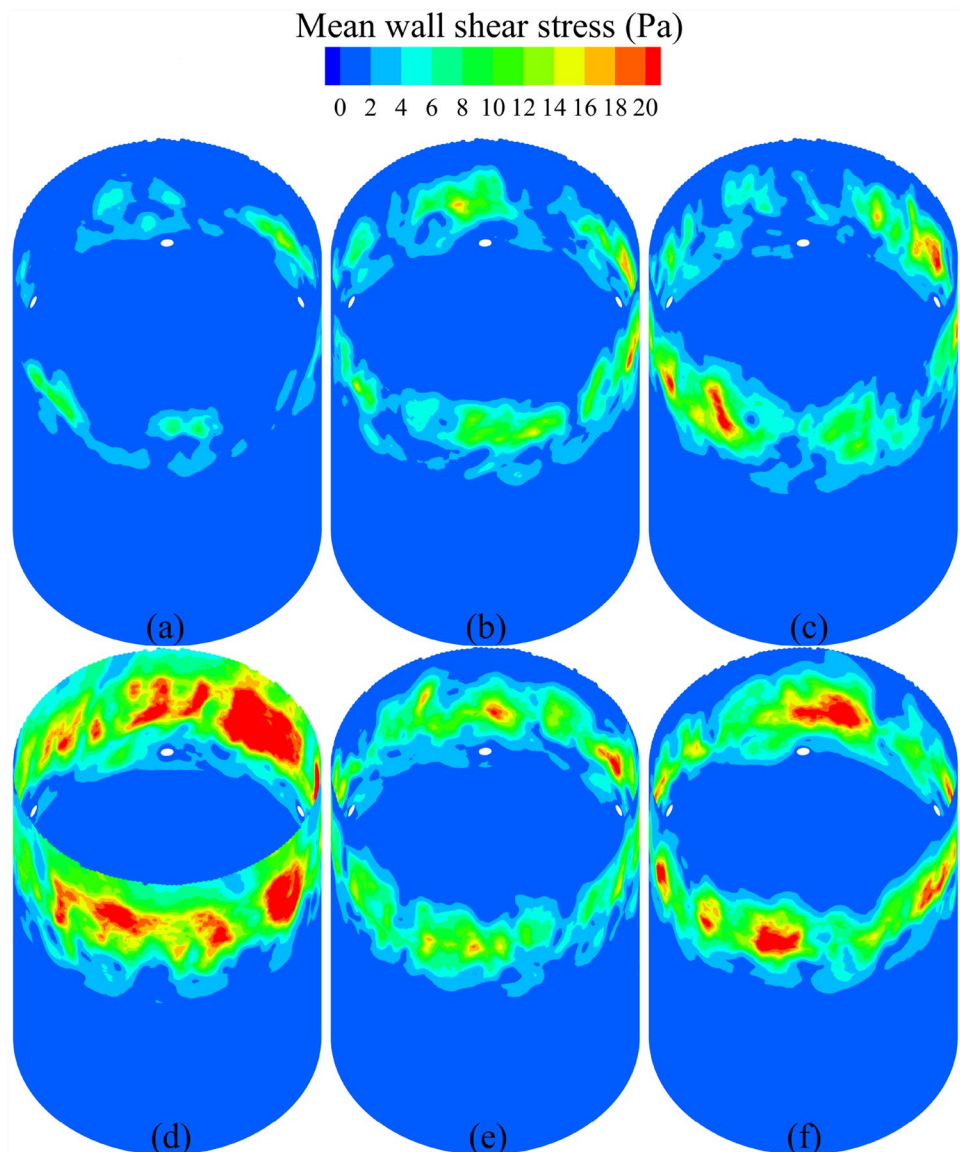
Declarations

Conflict of interest The authors declare that they have no conflict of interest.

References

1. Yang SJ, Zhang LW, Yu DH (2012) Intensive development and comprehensive utilization of metallurgical slag. In: Proceedings of CEABM 2012, Yantai.

2. Wan XB, Taskinen P, Shi JJ, Jokilaakso A (2021) A potential industrial waste-waste co-treatment process of utilizing waste SO_2 gas and residue heat to recover Co, Ni, and Cu from copper smelting slag. J Hazard Mater 414:125541. https://doi.org/10.1016/j.jhazmat.2021.125541

3. Li SW, Pan J, Zhu DQ, Guo ZQ, Shi Y, Dong T, Lu SH, Tian HY (2021) A new route for separation and recovery of Fe, Al and Ti from red mud. Resour Conserv Recycl 168:105314. https://doi.org/10.1016/j.resconrec.2020.105314

4. Lu GW, Zhang TA, Ma LN, Wang YA, Zhang WG, Zhang ZM (2019) Utilization of Bayer red mud by a calcification-carbonation method using calcium aluminate hydrate as a calcium source. Hydrometallurgy 188:248–255. https://doi.org/10.1016/j.hydromet.2019.05.018

5. Shen HT, Forssberg E (2003) An overview of recovery of metals from slags. Waste Manage 23(10):933–949. https://doi.org/10.1016/S0956-053X(02)00164-2

6. Guo ZQ, Zhu DQ, Pan J, Zhang F (2018) Innovative methodology for comprehensive and harmless utilization of waste copper slag

via selective reduction-magnetic separation process. J Clean Prod 187:910–922. https://doi.org/10.1016/j.jclepro.2018.03.264

7. Chen MS, Han ZR, Wang LZ (2011) Recovery of valuable metals from copper slag by hydrometallurgy. In: Proceedings of ICC-MME 2011, Beihai.

8. Li SW, Guo ZQ, Pan J, Zhu DQ, Dong T, Lu SH (2021) Stepwise utilization process to recover valuable components from copper slag. Minerals 11(2):211. https://doi.org/10.3390/min11020211

9. Erdenebold U, Choi HM, Wang JP (2018) Recovery of pig iron from copper smelting slag by reduction smelting. Arch Metall Mater 63(4):1793–1798. https://doi.org/10.24425/amm.2018.125106

10. Wang JP, Erdenebold U (2020) A study on reduction of copper smelting slag by carbon for recycling into metal values and cement raw material. Sustainability 12(4):1421. https://doi.org/10.3390/su12041421

11. Sarfo P, Das A, Wyss G, Young C (2017) Recovery of metal values from copper slag and reuse of residual secondary slag. Waste Manage 70:272–281. https://doi.org/10.1016/j.wasman.2017.09.024

12. Zhang BJ, Niu LP, Zhang TA, Li ZQ, Zhang DL, Zheng C (2017) Alternative reduction of copper matte in reduction process of copper slag. ISIJ Int 57(5):775–781. https://doi.org/10.2355/isijinternational.ISIJINT-2016-631

13. Zhao HL, Xiao YD, Liu FQ, Sohn HY (2021) Computational fluid dynamics simulation of gas-matte-slag three-phase flow in an ISASMELT furnace. Metall Mater Trans B 52(6):3767–3776. https://doi.org/10.1007/s11663-021-02290-8

14. Zhu S, Zhao QY, Liu Y, Zheng MZ, Li XL, Zhang TA (2021) Mixing behavior in a side-blown vortex smelting reduction reactor. Metall Mater Trans B 52(6):4082–4095. https://doi.org/10.1007/s11663-021-02326-z

15. Zhu S, Zhao QY, Liu Y, Li XL, Zhang TA (2022) Local bubble characteristics in a side-blown vortex smelting reduction reactor. Metall Mater Trans B 53(4):2303–2320. https://doi.org/10.1007/s11663-022-02530-5

16. Stephens D, Tabib M, Schwarz MP, Davis M (2012) CFD simulation of bath dynamics in the HIsmelt smelt reduction vessel for iron production. Prog Comput Fluid Dyn 12(2/3):196–206. https://doi.org/10.1504/PCFD.2012.047462

17. Witt PJ, Feng YQ, Davis MP (2014) Modelling thermal effects in the molten iron bath of the HIsmelt reduction vessel. In: Selected papers from 10th International Conference on Computational Fluid Dynamics in the Oil & Gas, Metallurgical and Process Industries, Trondheim.

18. Feng KF, Zhang JY, Wang B, Xu J, Xie JY, Cheng WL, Yin DY, Zheng SB (2014) Numerical simulation study on immersed side-blowing in C-H_2 smelting reduction furnace. In: Proceedings of 5th international symposium on high-temperature metallurgical processing, San Diego.

19. Bölke K, Ersson M, Imris M, Jönsson PG (2018) Importance of the penetration depth and mixing in the IRONARC process. ISIJ Int 58(7):1210–1217. https://doi.org/10.2355/isijinternational.ISIJINT.2018-043

20. Svantesson JL, Ersson M, Jönsson PG (2021) Effect of Froude number on submerged gas blowing characteristics. Materials 14(3):627. https://doi.org/10.3390/ma14030627

21. He YB, Guo WK, Li YH, Liu GM, Cui X (2022) Numerical simulation of flow characteristics of side-bottom combined blowing in iron bath reactor. J Iron Steel Res Int. https://doi.org/10.1007/s42243-022-00812-5

22. Sun MF, Zhang HB, Zhang JY, Wang B (2022) Research on mixing behavior in a combined top-bottom-side blown iron bath gasifier. Processes 10(5):973. https://doi.org/10.3390/pr10050973

23. Bian ZW, Chen DS, Sun LQ, Wang LN, Zhao HX, Zhen YL, Qi T (2023) Numerical simulation of multiphase flow in ironmaking process for oxygen-rich side-blown bath smelting furnace. Metall Mater Trans B. https://doi.org/10.1007/s11663-023-02766-9

24. Odenthal HJ, Thiedemann U, Falkenreck U, Schlueter J (2010) Simulation of fluid flow and oscillation of the argon oxygen decarburization (AOD) process. Metall Mater Trans B 41(2):396–413. https://doi.org/10.1007/s11663-009-9335-y

25. Wuppermann C, Rückert A, Pfeifer H, Odenthal HJ (2013) Physical and mathematical modeling of the vessel oscillation in the AOD process. ISIJ Int 53(3):441–449. https://doi.org/10.2355/isijinternational.53.441

26. Wei JH, He Y, Shi GM (2011) Mathematical modeling of fluid flow in bath during combined side and top blowing AOD refining process of stainless steel: application of the model and results. Steel Res Int 82(6):693–702. https://doi.org/10.1002/srin.201000279

27. Wei JH, He Y, Shi GM (2011) Mathematical modeling of fluid flow in bath during combined side and top blowing AOD refining process of stainless steel: mathematical model of the fluid flow. Steel Res Int 82(6):703–709. https://doi.org/10.1002/srin.201000278

28. Wimmer E, Kahrimanovic D, Pastucha K, Voraberger B, Wimmer G (2020) Computational fluid dynamics simulations for understanding and optimizing the AOD converter. Berg Huettenmaenn Monatsh 165(1):3–10. https://doi.org/10.1007/s00501-019-00938-2

29. Cheng ZF, Wang YN, Dutta A, Blanpain B, Guo MX, Malfliet A (2023) Numerical study of fluid flow and mixing in the argon oxygen decarburization (AOD) process. ISIJ Int 63(3):492–503. https://doi.org/10.2355/isijinternational.ISIJINT-2022-418

30. Chibwe DK, Akdogan G, Aldrich C, Taskinen P (2013) Modelling of mixing, mass transfer and phase distribution in a Peirce–Smith converter model. Can Metall Q 52(2):176–189. https://doi.org/10.1179/1879139512Y.0000000056

31. Chibwe DK, Akdogan G, Taskinen P, Eksteen JJ (2015) Modelling of fluid flow phenomena in Peirce–Smith copper converters and analysis of combined blowing concept. J S Afr Inst Min Metall 115(5):363–374. https://doi.org/10.17159/2411-9717/2015/v115n5a4

32. Chibwe DK, Akdogan G, Bezuidenhout GA, Kapusta JPT, Bradshaw S, Eksteen JJ (2015) Sonic injection into a PGM Peirce-Smith converter: CFD modelling and industrial trials. J S Afr Inst Min Metall 115(5):349–354. https://doi.org/10.17159/2411-9717/2015/v115n5a2

33. Almaraz A, López C, Arellano I, Barrón MA, Jaramillo D, Reyes F, Plascencia G (2014) CFD modelling of fluid flow in a Peirce–Smith converter with more than one injection point. Miner Eng 56:102–108. https://doi.org/10.1016/j.mineng.2013.11.001

34. Silva WM, Ribeiro BAB, Elias FT (2014) Simulation of the gas flow in a Peirce-Smith converter. In: Celebrating the megascale: Proceedings of the extraction and processing division symposium on pyrometallurgy in honor of David G.C. Robertson, San Diego.

35. Zhao HL, Zhao X, Mu LZ, Zhang LF, Yang LQ (2019) Gas-liquid mass transfer and flow phenomena in a Peirce–Smith converter: a numerical model study. Int J Miner Metall Mater 26(9):1092–1104. https://doi.org/10.1007/s12613-019-1831-8

36. Lu TT, Xiao YD, Zhou YG, Su QQ, Wei T, Liu FQ, Zhao HL (2021) Numerical simulation of nozzle height on the effect of fluid flow in a Peirce–Smith converter. JOM 73(10):2938–2945. https://doi.org/10.1007/s11837-021-04813-9

37. Zhang HL, Zhou CQ, Bing WU, Chen YM (2015) Numerical simulation of multiphase flow in a Vanyukov furnace. J S Afr Inst Min Metall 115(5):457–463. https://doi.org/10.17159/2411-9717/2015/v115n5a14

38. Liu GT, Liu Y, Li XL, Zhang TA (2016) Numerical simulation on multiphase flow in the two side-blown oxygen-enriched copper smelting furnace. In: Proceedings of TMS 2016, Nashville.

39. Liu YT, Yang TZ, Chen Z, Zhu ZY, Zhang L, Huang Q (2020) Experiment and numerical simulation of two-phase flow in oxygen enriched side-blown furnace. Trans Nonferrous Met Soc China 30(1):249–258. https://doi.org/10.1016/S1003-6326(19)65196-4

40. Xiao YD, Lu TT, Zhou YG, Su QQ, Mu LZ, Wei T, Zhao HL, Liu FQ (2021) Computational fluid dynamics study on enhanced circulation flow in a side-blown copper smelting furnace. JOM 73(9):2724–2732. https://doi.org/10.1007/s11837-021-04800-0

41. Wang Q, Jia SY, Tan FG, Li GQ, Ouyang DG, Zhu SH, Sun W, He Z (2021) Numerical study on desulfurization behavior during Kanbara reactor hot metal treatment. Metall Mater Trans B 52(2):1085–1094. https://doi.org/10.1007/s11663-021-02080-2